PERGAMON International Journal of Impact Engineering 25 (2001) 993–1022

INTERNATIONAL JOURNAL OF IMPACT ENGINEERING

www.elsevier.com/locate/ijimpeng

Penetration of 6061-T6511 aluminum targets by ogive-nosed VAR 4340 steel projectiles at oblique angles: experiments and simulations

Thomas L. Warren[a,*], Kevin L. Poormon[b]

[a] *Sandia National Laboratories, PO Box 5800, Albuquerque, NM 87185-1174, USA*
[b] *University of Dayton Research Institute, 300 College Park Avenue, Dayton, OH 45469-0182, USA*

Received 18 October 2000; received in revised form 14 May 2001

Abstract

In this paper we present the results from a combined experimental, analytical, and computational penetration program. First, we conducted a series of depth-of-penetration experiments using 0.021 kg, 7.11 mm diameter, 71.12 mm long, vacuum-arc-remelted 4340 ogive-nose steel projectiles. These projectiles were launched with striking velocities between 0.5 and 1.3 km/s using a 20 mm powder gun into 254 mm diameter, 6061-T6511 aluminum targets with angles of obliquity of 15°, 30°, and 45°. Next, we employed the initial conditions obtained from the experiments with a new technique that we have developed to calculate permanent projectile deformation without erosion. With this technique we use an explicit, transient dynamic, finite element code to model the projectile and an analytical forcing function derived from the dynamic expansion of a spherical cavity (which accounts for compressibility, strain hardening, strain-rate sensitivity, and a finite boundary) to represent the target. Results from the simulations show the final projectile positions are in good agreement with the positions obtained from post-test radiographs. Published by Elsevier Science Ltd.

1. Introduction

Currently both analytical and computational modeling of oblique penetration is an active field of research. When a long rod projectile strikes a target at an oblique angle, it experiences asymmetric loading which produces bending moments and stresses in the projectile that cause it to rotate. Furthermore, when obliquity is coupled with both pitch and yaw (pitch being in the plane of the angle of obliquity) the event is fully three dimensional and a fully numerical solution of the

*Corresponding author. Fax: +1-505-844-2563.
E-mail address: tlwarre@sandia.gov (T.L. Warren).

0734-743X/01/$ - see front matter Published by Elsevier Science Ltd.
PII: S0734-743X(01)00024-0

Nomenclature

a	cavity radius;
$\dot{a}$	cavity expansion velocity;
b	elastic–plastic interface position;
c_1	constant term nodal pressure coefficient;
c_2	linear term nodal pressure coefficient;
c_3	quadratic term nodal pressure coefficient;
d	position of dilational wave front or free surface;
f	decay function;
g	flow stress;
i	tensor indice;
j	tensor indice;
m	strain rate sensitivity exponent;
n	strain hardening exponent;
$\vec{n}$	unit outward normal vector;
p	hydrostatic pressure;
p_I	pressure at node I
r	radial Eulerian coordinate;
s_{ij}	deviatoric stress tensor;
t	time;
u	partical displacement;
A	constant term dimensionless fitting coefficient;
B	linear term dimensionless fitting coefficient;
C	quadratic term dimensionless fitting coefficient;
E	Young's modulus;
I	integer variable with range 1–4 corresponding to element side nodes;
K	bulk modulus;
$\vec{V}_1$	velocity vector at node I ;
V_s	striking velocity of the projectile;
Y	quasi-static yield strength of target material;
Y_p	quasi-static yield stress of the penetrator material;
δ_{ij}	Kronecker delta;
ε_{ii}	volumetric strain;
ε_p	effective plastic strain;
ε_{p0}	reference plastic strain;
$\dot{\varepsilon}_p$	effective plastic strain rate;
$\dot{\varepsilon}_{p0}$	reference plastic strain rate;
ε_r	radial strain;
ε_θ	tangential strain;
v	Poisson's ratio;
ρ	density of deformed material;

ρ_o	density of the undeformed target material;
ρ_{p}	density of the undeformed projectile material;
σ_{ij}	Cauchy stress tensor;
σ_{r}	radial stress;
σ_θ	hoop stress;
$\bar{\sigma}$	Von-Mises effective stress;
υ	partical velocity;
ψ	caliber-radius-head (CRH);

problem still poses extreme calculational difficulties. For further details on the subject of oblique impact the reader is referred to the recent review article by Goldsmith [1] that provides an extensive survey, which summarizes past and present experimental, analytical, and computational work on the subject.

Analytical methods for penetration mechanics began with the work of Bishop et al. [2]. They developed equations for the quasi-static expansion of cylindrical and spherical cavities and used these equations to estimate forces on conical nose punches pushed slowly into metal targets. Later, Goodier [3] developed a model to predict the penetration depth of rigid spheres launched into metal targets. That penetration model included target inertial effects, so Goodier [3] approximated the target response by results from the dynamic, spherically symmetric, cavity-expansion equations for an incompressible target material derived by Hill [4] and discussed by Hill [5] and Hopkins [6]. More recently, Forrestal et al. [7], Forrestal et al. [8], Forrestal et al. [9], Warren and Forrestal [10], Piekutowski et al. [11] developed spherical cavity-expansion penetration models for rigid projectiles that penetrate ductile metal targets. They developed closed-form expressions for the depth of penetration of rigid projectiles with different nose shapes and demonstrated good agreement with experimental results for normal impact.

Roisman et al. [12] recently performed oblique penetration experiments in order to validate the analytical penetration model developed by Roisman et al. [13]. In their penetration experiments they launched hard tungsten sinter alloy, ogive-nosed rods into 6061-T651 aluminum plate targets with striking velocities between 0.5 and 0.7 km/s and angles of obliquity of 0°, 30° and 45°. With their model they assume the projectile is rigid and target to be rigid-perfectly plastic in the plastic region and linear elastic in the elastic region. Their theoretical results show good agreement with the experiments provided the projectile can be assumed to be rigid; however, if the projectile bends they overpredict the final depth of penetration.

Throughout the twentieth century there has been considerable effort and progress in the development of various computer codes (based on different representations of the conservation laws for a continuum: Lagrangian, Eulerian, Arbitrary Lagrangian–Eulerian, etc.) that serve as powerful and versatile computational tools which are used to solve complex problems. A detailed summary and survey that discusses several of the more widely used computer codes for high velocity impact is given by Zukas [14]. However, at present, the time required to complete a single fully three dimensional penetration run is still excessive and prohibits any prospect for streamlining the penetration analysis for use in an overall design tool that would permit numerous simulations.

Recently, Warren and Tabbara [15] employed a new technique to simulate experiments performed by Forrestal and Piekutowski [16] in which spherical-nosed 4340 steel projectiles penetrated 6061-T6511 aluminum targets at normal incidence with pitch and yaw. In this study good agreement was obtained for projectile deformation and final depth of penetration. With this new technique [17] we use an explicit transient dynamic finite element code to model the projectile and an analytical forcing function derived from the dynamic expansion of a spherical cavity to represent the target. This methodology eliminates the need for discretizing the target as well as the need for a contact algorithm, which reduces the computer time and memory requirements. Furthermore, this method avoids the problems due to excessive mesh distortion associated with Lagrangian formulations as discussed by Camacho and Ortiz [18]. The method does however suffer from a disadvantage if the tail of the projectile continues to significantly whip back and forth well into the tunneling region. In this case the simulation method loses accuracy due to the fact the current cavity expansion algorithm applies a load on the shank whenever there is a component of velocity in the outward normal direction and does not account for material that has been moved out of the way in the tunneling region.

The method employed by Warren and Tabbara [15] gave good results provided free surface effects are minimal which is the case for normal incidence with small angles of pitch and yaw. However, as angle of obliquity is increased free surface effects become more significant as will be shown in this paper. Recently, Macek and Duffey [19] used a spherical cavity expansion forcing function derived for a cavity of finite size to account for near-surface effects in the penetration of geologic media. With their forcing function they consider the target to be an incompressible, damaged Mohr–Coulomb material, and as they point out it is essential to assume incompressibility because without this assumption time dependent wave propagation and reflections would need to be tracked relative to the moving penetrator. The use of a fully incompressible forcing function however will cause an over prediction of the target resistance [10]. An alternative method to address free surface effects has been proposed by Longcope et al. [20]. With their method they require the forcing function acting on the surface of the penetrator to depend on a nondimensional distance to the free surface, d^*/a as shown in Fig. 1. The distance d^* is taken from a surface node to the free surface along a normal to the penetrator surface and a is a radius, characteristic of the local penetrator geometry at the node (it is noted that in our analysis we use $d = d^* + a$ instead of d^* to define the distance to the free surface). The loading on the penetrator is taken to be zero if d^*/a is less than a critical value (which is obtained empirically or from the analysis of a spherical cavity expanding quasistatically in a finite sphere of the target material) otherwise it is the full cavity expansion pressure. This method however neglects inertia effects which are shown in this paper to increase with cavity expansion velocity.

In the present study we conducted a suite of depth-of-penetration experiments using ogive-nose, steel, long rod projectiles and 6061-T6511 aluminum targets. The projectiles were launched with striking velocities between 0.5 and 1.3 km/s and angles of obliquity of 15°, 30°, and 45°. Next, we used the initial conditions obtained from the experiments with the simulation technique outlined by Warren and Tabbara [17] with modifications to account for the free surface effects encountered during oblique penetration. These modifications involve constructing a decay function that is based on the solution of a dynamically expanding spherical cavity in a finite sphere of target material which is assumed to be incompressible and perfectly plastic. We then multiply the cavity expansion pressure used by Warren and Tabbara [15] (which accounts for compressibility, strain

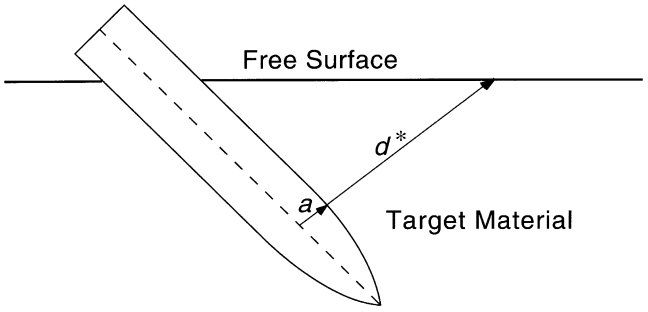

Fig. 1. Geometry of the free surface effect model.

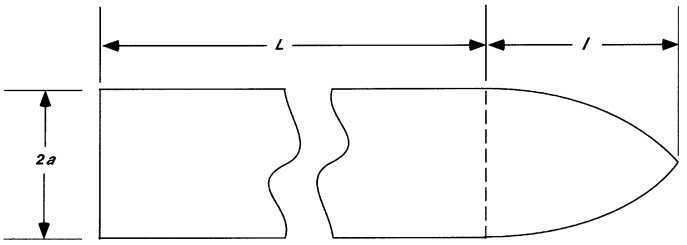

Fig. 2. Geometry for the ogive-nose rod with a 3.0 caliber-radius-head (CRH), $L = 59.3$ mm, $l = 11.8$ mm, and $2a = 7.11$ mm.

hardening, and strain-rate sensitivity) by the decay function in order to account for the free surface effects. Results from the simulations are compared with the final projectile configurations obtained from post-test radiographs.

2. Experiments

The dimensions of the ogive-nose, steel projectiles used in this series of penetration experiments are given in Fig. 2. The projectile material was vacuum-arc-remelted (VAR) 4340 steel [21] that had an approximate nominal hardness of $R_c = 44.5$, tensile yield strength of 1430 MPa, and fracture toughness of 104 MPa $(m)^{1/2}$. Hardness measurements were taken at the center of a piece cut from the projectile rod material adjacent to where the projectile nose was machined. The 6061-T6511 aluminum targets were 254 mm in diameter with the face of the target machined at angles of 15°, 30°, and 45° as illustrated in Fig. 3. The lengths of the targets were determined to be the sum of the maximum anticipated depth of penetration plus the length of the rod. The targets were installed in the target chamber with the angle of obliquity of the target face in the $X-Y$ plane as shown in Fig. 3. Target obliquity angles were aligned relative to the projectile trajectory using a laser beam that was aligned to the gun bore and a mirror that was set at a complementary angle. The mirror was placed on the target face and reflected the laser beam back onto itself when the target was properly aligned.

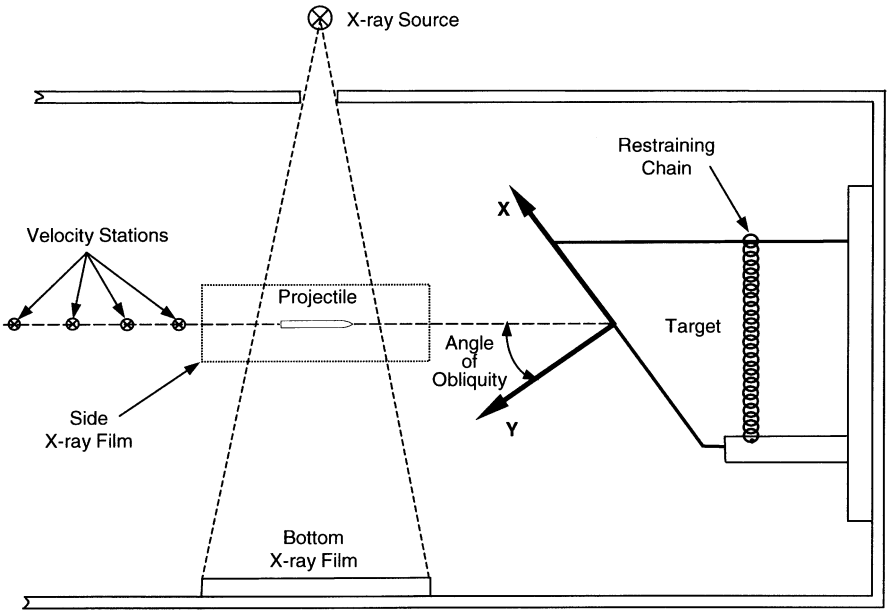

Fig. 3. Experimental configuration.

The projectiles were encased in a plastic sabot and launched using a 20 mm powder gun. After exiting the muzzle, aerodynamic pressure separated the sabot from the projectile. A steel sabot stripper plate with a small hole aligned to the projectile trajectory was located a few feet in front of the target. The plate stripped away the sabot preventing it from striking the target. Projectile striking velocities were measured with an accuracy of better than 0.5% using four laser-photodetector stations installed at various locations along the flight path. The pitch and yaw of the projectile were obtained from radiographs obtained with use of an orthogonal pair of 150 kV flash X-rays positioned in front of the face of the target. The final depth of penetration and shape of the projectile were determined, after each test, from a radiograph of a 38 mm thick slice of the target. The slice was cut from each target along vertical planes parallel to the projectile flight path. Table 1 summarizes the penetration data from the experiments.

3. Spherical cavity expansion model and numerical simulation

In this section, we develop an expression that approximates the target response with results from a dynamic, spherically symmetric cavity-expansion problem. This involves obtaining an approximate expression for the radial stress at a cavity surface that accounts for compressibility, strain hardening, strain-rate sensitivity, and a finite boundary. We then employ this expression for radial stress with the computational procedure developed by Warren and Tabbara [17] for obtaining the trajectory and final spatial configuration of a projectile.

In the work by Forrestal et al. [7] with steel rods penetrating aluminum targets it was observed from photomicrographs that there was 5–15 μm layer normal to the tunnel surface that had

Table 1
Penetration data for VAR 4340, $R_c = 44.5$, 3-CRH-nosed, steel rods (Targets were 254 mm diameter bars of 6061-T6511 aluminum with lengths shown below. For Pitch, D = Down and U = Up. For Yaw, R = Right and L = Left)

Shot number	Striking velocity, V_S (m/s)	Penetration[a] (mm)	Mass (g)	Penetrator Hardness R_C	Pitch (°)	Yaw (°)	Target length (m)
45° Target							
1-0468	1184	217	20.452	44.6	0.50 U	0.75 L	0.236
1-0467	963	168[b]	20.454	44.7	0.75 U	1.00 R	0.236
1-0466	802	109[c]	20.475	44.5	2.00 U	1.50 L	0.219
1-0465	553	37[d]	20.456	44.3	1.25 U	0.75 R	0.227
30° Target							
1-0453	1156	188	20.448	44.4	3.25 U	0	0.236
1-0451	853	108	20.469	44.5	2.75 U	0.75 L	0.236
1-0450	753	91	20.450	44.9	0.75 D	0.25 L	0.236
1-0463	577	62	20.475	44.6	0.50 D	0.75 L	0.236
15° Target							
1-0447	1209	213	20.457	44.5	0.75 U	0.50 L	0.284
1-0445	985	136	20.478	44.5	2.50 U	0.75 L	0.183
1-0461	759	92	20.443	44.4	0.50 U	0.75 L	0.183
1-0462	590	60	20.456	44.2	0.50 D	0.50 R	0.183

[a] Depth of penetration measured along the channel path to the *point* of the projectile.
[b] Projectile nose exited front face of target 145 mm below the entrance hole measured along the target face. Exit angle was 95–100° to the shot-line axis. 12 mm of projectile nose protruding from target.
[c] Projectile exited front face of target 99 mm below the entrance hole measured along the target face. Exit angle was 90–95° to the shot-line axis and exit velocity is estimated at 80 m/s. Bent rod recovered.
[d] Projectile exited front face of target 40 mm below the entrance hole measured along the target face. Exit angle was 85–90° to the shot-line axis and exit velocity is estimated at 300 m/s. Bent rod recovered.

undergone microstructural changes consistent with very localized melting. Furthermore, a simple transient heat conduction analysis considering heat transferring into a semiinfinite solid indicates heat will transfer only very short distance into the plastic region at this size scale due to the short event time. These results are further substantiated by the recent detailed computational work of Camacho and Ortiz [18]. Camacho and Ortiz [18] performed finite-element simulations corresponding to experiments conducted by Forrestal et al. [22] on the perforation of 5083-H131 aluminum plates with tungsten, conical-nosed projectiles. These simulations use a new adaptive meshing technique and a constitutive material law that includes rate-dependent plasticity, heat conduction, and thermal–mechanical coupling. They conclude there is an exceedingly thin melted layer in the target next to the projectile that provides a nearly frictionless interface. Therefore, based on these results we neglect both sliding frictional resistance at the projectile–target interface along with thermal softening effects in the target material due to heat conduction at the projectile–target interface, and feel these are reasonable assumptions for the striking velocities considered in this work.

3.1. Spherical cavity expansion model

To obtain the target response function we consider the expansion of a spherically symmetric cavity from zero initial radius to radius a. As shown in Fig. 4, this expansion produces plastic and elastic response regions. The plastic region is bounded by the radii $r = a$ and $r = b$, where r is the radial Eulerian coordinate and b is the interface position between the plastic and elastic response regions. Similarly, the elastic region is bounded by $r = b$ and $r = d$, where d corresponds to the position of the dilatational wave front or free surface. Next, we present the equations that govern this problem and derive our solution.

The equations of momentum and mass conservation in Eulerian coordinates with spherical symmetry are

$$\frac{\partial \sigma_r}{\partial r} + \frac{2(\sigma_r - \sigma_\theta)}{r} = -\rho\left(\frac{\partial v}{\partial t} + v\frac{\partial v}{\partial r}\right), \tag{1a}$$

$$\rho_o \frac{\partial}{\partial r}[(r-u)^3] = 3\rho r^2, \tag{1b}$$

where σ_r, σ_θ are the radial and hoop components of the Cauchy stress, measured positive in compression, and ρ_o and ρ are the densities in the undeformed and deformed states and are equal when the material is assumed incompressible. Particle displacement u and particle velocity v in the radial direction (outward motion taken positive) are related by

$$\frac{\partial u}{\partial t} = v\left(1 - \frac{\partial u}{\partial r}\right). \tag{2}$$

The solution to the dynamic, spherically symmetric cavity-expansion problem with compressibility is contingent on the use of a similarity variable [23]. This requires the cavity to be opened from a zero initial radius at a constant velocity in an infinite domain. Using the similarity variable in the equations of mass and momentum conservation given by (1) transforms the system of nonlinear partial differential equations into a system of nonlinear ordinary

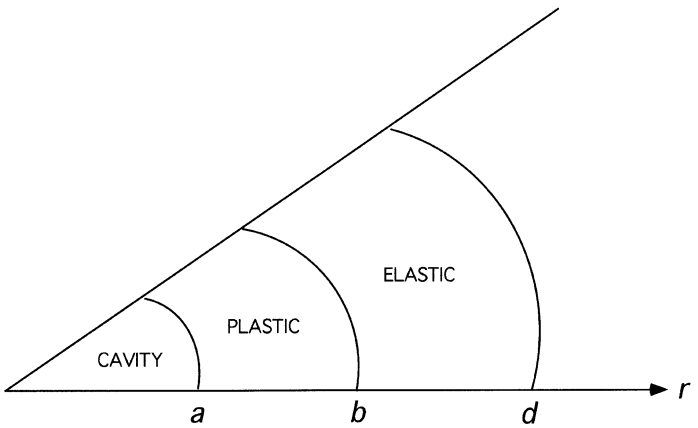

Fig. 4. Response regions for the cavity-expansion problem.

differential equations. This system is then solved numerically to obtain the radial stress at a cavity surface as a function of cavity expansion velocity. Details of the dynamic, spherically symmetric cavity-expansion solution that accounts for compressibility, strain hardening, and strain-rate sensitivity are given by Warren and Forrestal [10], and only the final result will be presented here. Using a least squares fit to the numerical data allows the radial stress at the cavity surface to be accurately represented by a function of the form

$$\frac{\sigma_{\mathrm{r}}(a)}{Y} = A + B\left(\sqrt{\frac{\rho_o}{Y}}\,\dot{a}\right) + C\left(\sqrt{\frac{\rho_o}{Y}}\,\dot{a}\right)^2, \tag{3}$$

where $(\dot{\cdots}) \equiv \mathrm{d}(\cdots)/\mathrm{d}t$ (i.e. material derivative operator), $\dot{a}$ is the cavity expansion velocity, Y is the quasi-static yield strength of the target material, and A, B, and C are dimensionless fitting coefficients. Warren and Forrestal [10] give the parameters in (3) for 6061-T6511 aluminum that account for compressibility, strain hardening, and strain-rate sensitivity. These values are summarized in Table 2. The constitutive model used for the target material in [10] was fit to compressive stress–strain data at strain rates between 10^{-3} and 10^5 1/s. Adiabatic heating of the material due to plastic deformation was not accounted for explicitly; however, some of this is swept into the model through curve fitting of the experimental data. Additionally, experimental stress–strain data for the 6061-T6511 aluminum rounds indicated minor anisotropy for strains less than 25% as shown in [10]; however, for the model we assumed the material to be isotropic.

Next, we obtain the solution for the dynamic, spherically symmetric cavity-expansion problem with a finite boundary. For this problem we assume the material is perfectly plastic and incompressible. The assumption of incompressibility allows the equation for conservation of mass given by (1b) to be directly integrated to give the radial particle displacement as

$$u = r\left[1 - \left(1 - \frac{a^3}{r^3}\right)^{1/3}\right]. \tag{4}$$

Particle velocity in the radial direction is obtained by differentiating (4) and substituting into (2) giving

$$v = \frac{a^2\dot{a}}{r^2}, \tag{5}$$

where the cavity radius a is only a function of time. As discussed by Hill [5], the state of stress due to symmetry is just a hydrostatic tension superposed on a uniaxial compressive stress. Thus, the yield criterion for a perfectly plastic material is

$$\sigma_{\mathrm{r}} - \sigma_\theta = Y. \tag{6}$$

Table 2
6061-T6511 aluminum data

Y (MPa)	ρ_o (kg/m^3)	A	B	C
276	2710	5.0394	0.9830	0.9402

Using (5) and (6) in conservation of momentum (1a) and integrating throughout the plastic region $a \leqslant r \leqslant b$ gives the radial stress at the cavity surface as

$$\sigma_r(a) = \sigma_r(b) + 2Y \ln\left(\frac{b}{a}\right) - \rho\left[(\ddot{a}a^2 + 2a\dot{a}^2)\left(\frac{1}{b} - \frac{1}{a}\right) - \frac{a^4\dot{a}^2}{2}\left(\frac{1}{b^4} - \frac{1}{a^4}\right)\right]. \tag{7}$$

In the elastic region $b \leqslant r \leqslant d$ displacements and strains are assumed small. Response equations for the elastic region are presented by Hopkins [6]. The particle displacement and particle velocity in the radial direction are

$$u = \frac{a^3}{3r^2}, \quad \upsilon = \frac{a^2\dot{a}}{r^2}. \tag{8}$$

The elastic strains are

$$\varepsilon_r = -\frac{\partial u}{\partial r} = \frac{2a^3}{3r^3}, \quad \varepsilon_\theta = -\frac{u}{r} = -\frac{a^3}{3r^3} \tag{9}$$

and Hook's law for an incompressible material provides the relation

$$\sigma_r - \sigma_\theta = \frac{2Ea^3}{3r^3}, \tag{10}$$

where E is Young's modulus. Using (10) with (1a) and integrating throughout the elastic region $b \leqslant r \leqslant d$ gives the radial stress at the elastic–plastic interface as

$$\sigma_r(b) = \sigma_r(d) + \frac{4Ea^3}{9}\left(\frac{1}{b^3} - \frac{1}{d^3}\right) + \rho\left[(\ddot{a}a^2 + 2a\dot{a}^2)\left(\frac{1}{b} - \frac{1}{d}\right) - \frac{a^4\dot{a}^2}{2}\left(\frac{1}{b^4} - \frac{1}{d^4}\right)\right], \tag{11}$$

where $\sigma_r(d) = 0$ as $d \to \infty$ or becomes a free surface. For an incompressible material, the Hugoniot interface conditions require that the displacement, velocity, and traction normal to the elastic–plastic interface be continuous [6]. Equating (6) and (10) at the elastic–plastic interface gives

$$\frac{a}{b} = \left(\frac{3Y}{2E}\right)^{1/3} \tag{12}$$

Using (11) and (12) in (7) and considering the cavity to be opening at a constant velocity (i.e. $\ddot{a} = 0$) gives the radial stress at the cavity surface as

$$\sigma_r(a) = \frac{2Y}{3}\left[\ln\left(\frac{2E}{3Y}\right) + 1 - \frac{2E}{3Y}\left(\frac{a}{d}\right)^3\right] + \frac{\rho\dot{a}^2}{2}\left[3 + \left(\frac{a}{d}\right)^4 - 4\left(\frac{a}{d}\right)\right], \tag{13}$$

which is valid until the elastic-plastic boundary reaches the free surface (i.e. $d \geqslant b$). For subsequent expansion with $d < b$, the radial stress will steadily decrease as

$$\sigma_r(a) = 2Y \ln\left(\frac{d}{a}\right) + \frac{\rho\dot{a}^2}{2}\left[3 + \left(\frac{a}{d}\right)^4 - 4\left(\frac{a}{d}\right)\right], \tag{14}$$

which is the result given by Hill [5] if the inertia term is neglected. Plots of the radial stress as a function of d/a obtained from (13) and (14) for several expansion velocities are shown in Fig. 5. It is observed that free surface effects extend to larger distances as expansion velocity is increased.

We now construct a decay function, which allows us to employ the results from (13), and (14) with the expression given in (3) that accounts for compressibility, strain hardening, and strain-rate sensitivity in infinite medium. This is done by normalizing (13) and (14) with the result given by (13) letting $d \to \infty$. Thus,

$$f(d,a,\dot{a}) = \frac{2Y/3\left[\ln(2E/3Y) + 1 - 2E/3Y(a/d)^3\right] + \rho\dot{a}^2/2\left[3 + (a/d)^4 - 4(a/d)\right]}{2Y/3\left[1 + \ln(2E/3Y)\right] + 3/2(\rho\dot{a}^2)}, \quad d \geqslant b \tag{15a}$$

$$f(d,a,\dot{a}) = \frac{2Y\ln(d/a) + \rho\dot{a}^2/2\left[3 + (a/d)^4 - 4(a/d)\right]}{2Y/3\left[1 + \ln(2E/3Y)\right] + 3/2(\rho\dot{a}^2)}, \quad d < b \tag{15b}$$

where $0 \leqslant f(d,a,\dot{a}) \leqslant 1$. Using (15) with (3) gives

$$\frac{\sigma_r(a)}{Y} = \left[A + B\left(\sqrt{\frac{\rho_o}{Y}}\,\dot{a}\right) + C\left(\sqrt{\frac{\rho_o}{Y}}\,\dot{a}\right)^2\right] f(d,a,\dot{a}). \tag{16}$$

This result provides a solution that accounts for compressibility, strain hardening, and strain-rate sensitivity along with the effects of a finite boundary which is obtained through the analogous incompressible problem.

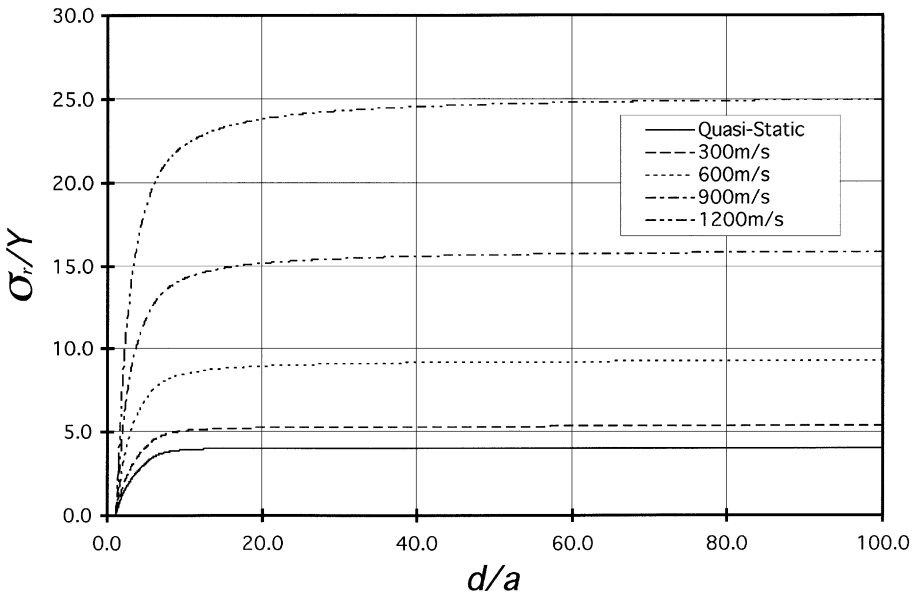

Fig. 5. Radial stress at the cavity surface vs. distance to the free surface obtained from the incompressible solution given by Eqs. (13) and (14).

3.2. Finite element method

The spherical cavity-expansion forcing function given by (16) has been implemented in the Sandia developed explicit transient dynamic finite element code PRONTO 3D [24] as a normal traction (or pressure) boundary condition that acts on a prescribed surface. In PRONTO 3D four nodal pressures are calculated for each element side (i.e. a side of a hexagonal continuum element or mid-surface of a structural shell element) that is included in a prescribed side set as shown in Fig. 6. These nodal pressures are obtained from

$$p_I = [c_1 + c_2(\vec{V}_I \bullet \vec{n}) + c_3(\vec{V}_I \bullet \vec{n})^2] f(d, a, \vec{V}_I \bullet \vec{n}) \quad (I = 1, 4), \tag{17}$$

where the dot represents a scalar product, $\vec{V}_I$ is the nodal velocity vector, $\vec{n}$ is the outward unit vector normal to the diagonals of the element side, and the constant nodal pressure coefficients are related to the dimensionless fitting coefficients in (16) as $c_1 = AY$, $c_2 = B(\rho_o Y)^{1/2}$, and $c_3 = C\rho_o$. In (17), the distance d is obtained by projecting a line segment from node I in the direction of $\vec{n}$ to the free surface and calculating its length. If the length of d is greater than $200a$, where a is the distance from the centerline of the undeformed penetrator in the direction of $\vec{n}$ to node I, then the free surface effect is neglected. The values of p_I are updated during each time increment using the current values of $\vec{V}_I$ and $\vec{n}$. If the scalar product $(\vec{V}_I \bullet \vec{n})$ at a node is zero, negative, or if the node lies outside the bounds of where the cavity-expansion forcing function is defined then the pressure is set to zero for that node. A set of consistent global forces arising from these pressures over an element side are calculated as discussed by Taylor and Flanagan [24]. These forces are accumulated into an applied load vector as each element side in the side set is considered. The applied load vector is then incorporated into the equations of motion for the body which are integrated using a modified central difference integration scheme as discussed by Taylor and Flanagan [24].

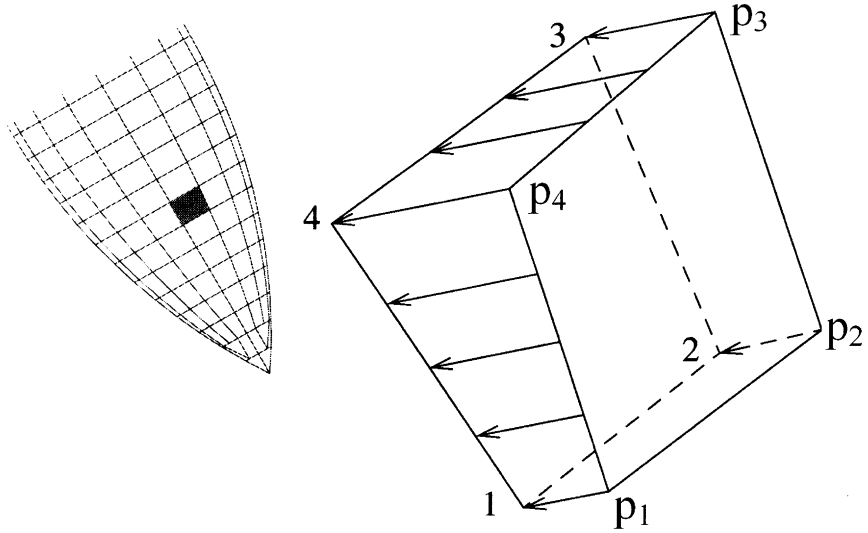

Fig. 6. Definition of a pressure boundary condition that acts on an element side.

The finite element mesh used to model the ogive-nosed projectiles in all of the simulations is illustrated in Fig. 7. This mesh is constructed with 2816 eight-node constant strain hexahedral continuum elements, and has a total of 3197 nodes.

3.3. Constitutive model for VAR 4340 steel

The constitutive equations used for modeling the projectile in PRONTO 3D assume that the volumetric (dilatational) response is governed by a pressure–volumetric strain relation while the shear (deviatoric) response obeys a conventional flow theory of plasticity. Decomposing the Cauchy stress tensor into hydrostatic and deviatoric components gives

$$\sigma_{ij} = -p\delta_{ij} + s_{ij}, \tag{18}$$

where p is the hydrostatic pressure, δ_{ij} is the Kronecker delta, and s_{ij} is the deviatoric stress tensor. The pressure–volumetric strain relation is

$$p = -\frac{1}{3}\sigma_{ii} = -K\varepsilon_{ii} = K\left(1 - \frac{\rho_{\mathrm{p}}}{\rho}\right), \tag{19}$$

where K is the bulk modulus, ε_{ii} is the volumetric strain, ρ_{p} is the density of the undeformed projectile material, and ρ is the density of the material in the deformed configuration.

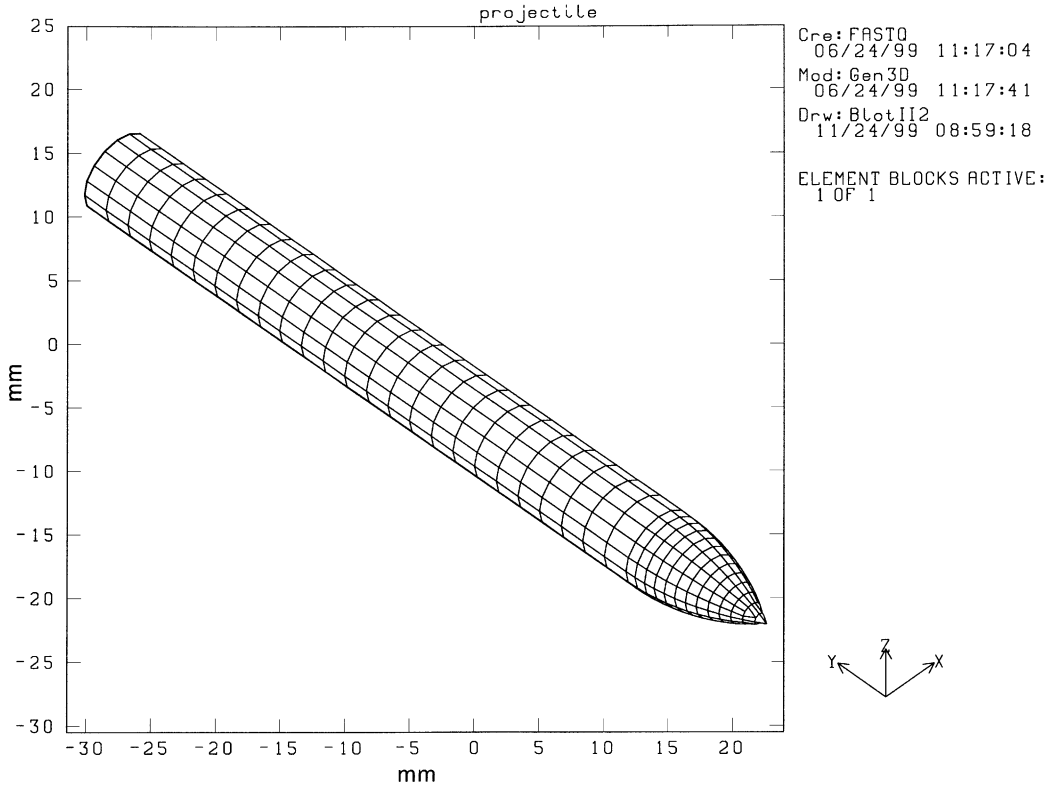

Fig. 7. Finite element mesh of a ogive-nose projectile.

Plastic flow is introduced through a Von-Mises elastic–viscoplastic material model similar to that used by Camacho and Ortiz [18]. With this model we assume the material is isotropic and that data from uniaxial tests can describe the multiaxial behavior through a relationship between Von-Mises effective stress and equivalent plastic strain and strain rate. As with the target material we neglect transient heat conduction due to the size scale and short event time. Additionally, the majority of the penetrator deformation occurs early in the penetration process which further justifies this assumption. We also neglect explicitly accounting for adiabatic heating due to plastic deformation. Some of this however is accounted for through the curve fitting to experimental data.

Effective plastic strain rate is defined through the power law relationship

$$\dot{\varepsilon}_{\mathrm{p}} = \dot{\varepsilon}_{\mathrm{p0}}\left[\left(\frac{\bar{\sigma}}{g(\varepsilon_{\mathrm{p}})}\right)^{m} - 1\right], \quad \bar{\sigma} \geqslant g(\varepsilon_{\mathrm{p}}), \tag{20a}$$

$$\dot{\varepsilon}_{\mathrm{p}} = 0, \quad \bar{\sigma} < g(\varepsilon_{\mathrm{p}}), \tag{20b}$$

where $\bar{\sigma} = \sqrt{3/2}(s_{ij}s_{ij})^{1/2}$ is the Von-Mises effective stress, g is the flow stress, ε_{p} is the effective plastic strain, $\dot{\varepsilon}_{\mathrm{p0}}$ is a reference plastic strain rate, and m is the strain rate sensitivity exponent. We also employ a power hardening law in which

$$g = Y_{\mathrm{p}}\left(1 + \frac{\varepsilon_{\mathrm{p}}}{\varepsilon_{\mathrm{p0}}}\right)^{1/n}, \tag{20c}$$

where n is the strain hardening exponent, $\varepsilon_{\mathrm{p0}}$ is a reference plastic strain, and Y_{p} is the quasi-static yield stress of the material. The constitutive model in (20) uses a rate tangent modulus method [25] for integration and was implemented in PRONTO 3D following the procedure described by Taylor and Flanagan [24] for adding new constitutive models.

Additionally, default values of hourglass control and artificial bulk viscosity are applied to the numerical solution as discussed by Taylor and Flanagan [24]. Hourglass control is required because PRONTO 3D uses one point integration of an element which under-integrates the element resulting in a rank deficiency which manifests itself into spurious zero energy modes (hourglass modes) that must be constrained. Artificial bulk viscosity is employed to prevent high velocity gradients from collapsing an element before it has a chance to respond and also to quiet truncation frequency ringing.

We obtained constants for the constitutive Eq. (20) from compressive true stress–strain data for VAR 4340 $R_{\mathrm{c}} = 45$ steel obtained by Ravichandran [26] at nominal strain rates [27] of 0.001, 0.1, 1643, 2313 and 4255 1/s, and also from pressure-shear data obtained by Ramesh [28] at a nominal strain rate of 115470 1/s. The model parameters were obtained from curve fits to these

Table 3
VAR 4340 steel data

VAR 4340	Y_{p} (MPa)	$\varepsilon_{\mathrm{p0}}$	$\dot{\varepsilon}_{\mathrm{p0}}$ (1/s)	n	m
$R_{\mathrm{c}} = 39$	1225	5.947×10^{-3}	5.940×10^{-4}	25.0	83.3
$R_{\mathrm{c}} = 45$	1481	7.189×10^{-3}	5.690×10^{-8}	25.0	139.3
$R_{\mathrm{c}} = 44.5$	1462	7.1×10^{-3}	5.690×10^{-8}	25.0	139.3

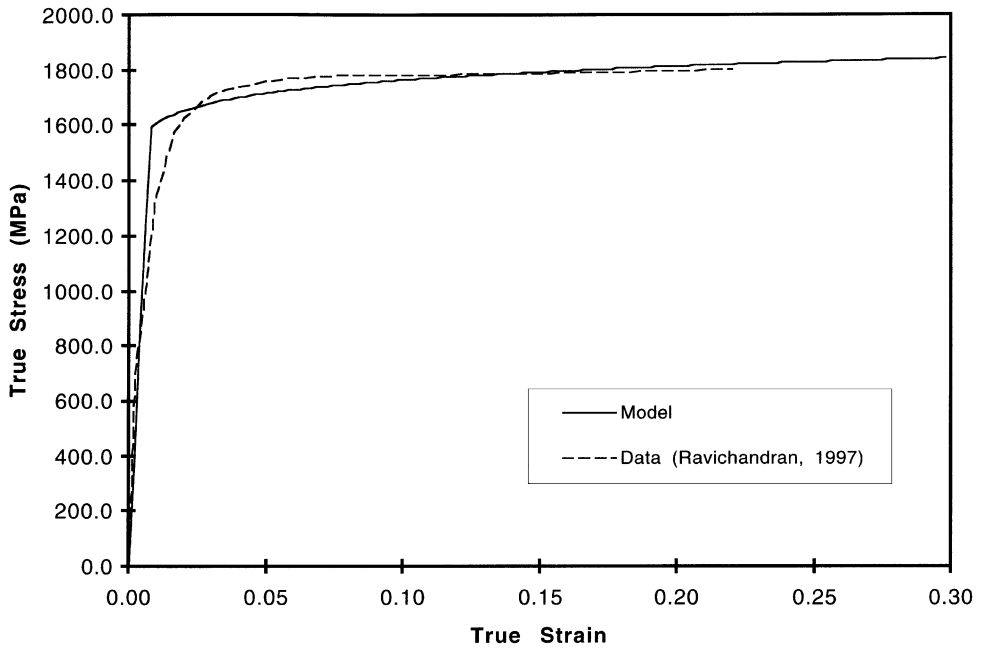

Fig. 8. True stress–strain data and data fit for VAR 4340 $R_c = 45$ steel at a nominal strain rate of $\dot{\varepsilon} = 0.001$ 1/s.

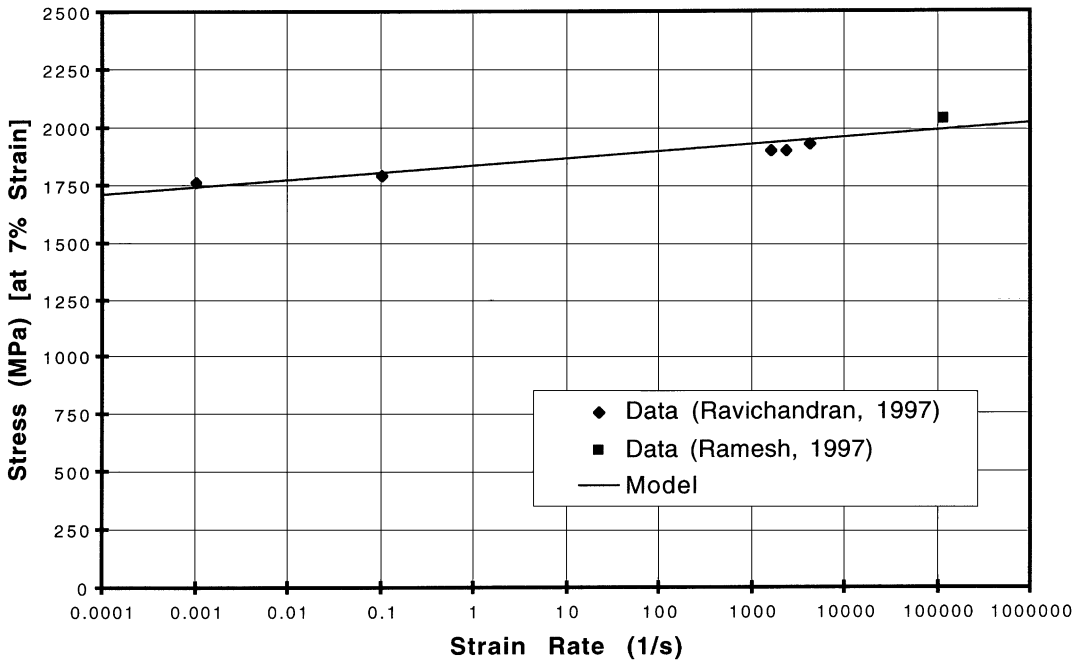

Fig. 9. Rate sensitivity diagram for VAR 4340 $R_c = 45$ steel at a fixed strain of 7%.

Table 4
Penetration results[a]

Striking velocity (m/s)	Angle of obliquity (°)	Pitch (°)	Yaw (°)	Experimental				SCE/PRONTO 3D with free surface effects				SCE/PRONTO 3D without free surface effects			
				Tip		Tail		Tip		Tail		Tip		Tail	
				X (mm)	Y (mm)	X (mm)	Y (mm)	X (mm)	Y (mm)	X (mm)	Y (mm)	X (mm)	Y (mm)	X (mm)	Y (mm)
1184	45	0.5 U	0.75 L	−203.3	−7.25	−141.3	−35.0	−190.0	−5.4	−127.4	−33.0	−185.0	−81.2	−116.6	−67.8
963	45	0.75 U	1.0 R	−149.9	8.63	−90.1	−24.5	−136.1	4.7	−75.5	−22.8	−129.7	−62.9	−63.2	−40.8
802	45	2.0 U	1.5 L	Projectile exited the target at $X = -100$				−104.3	−8.9	−36.1	−15.2	−91.4	−56.2	−30.0	−21.8
553	45	1.25 U	0.75 R	Projectile exited the target at $X = -40$				Projectile exited the target at $X = -38$				−51.5	−26.1	8.7	9.6
1156	30	3.25 U	0	−113.2	−149.5	−66.4	−96.8	−88.7	−138.1	−47.6	−77.6	−83.1	−133.8	−42.3	−72.5
853	30	2.75 U	0.75 L	−68.7	−83.4	−21.5	−32.3	−69.4	−97.1	−27.2	−40.0	−60.2	−96.3	−22.1	−35.8
753	30	0.75 D	0.25 L	−71.4	−55.2	−14.3	−15.0	−69.1	−65.2	−16.6	−18.6	−61.6	−73.5	−15.2	−2.0
577	30	0.5 D	0.75 L	−50.6	−35.4	5.7	5.0	−47.8	−42.8	4.6	3.3	−42.0	−50.2	4.5	2.8
1209	15	0.75 U	0.5 L	−70.5	−201.2	−45.7	−136.0	−63.2	−205.5	−40.9	−138.4	−68.6	−201.8	−42.6	−135.9
985	15	2.5 U	0.75 L	−39.1	−130.7	−17.6	−63.7	−29.9	−133.0	−14.8	−62.4	−32.8	−130.8	−15.0	−60.8
759	15	0.5 U	0.75 L	−34.4	−85.0	−7.1	−20.0	−30.4	−95.5	−8.8	−28.0	−29.5	−95.8	−8.5	−28.0
590	15	0.5 D	0.5 R	−26.1	−54.7	6.8	8.3	−22.2	−60.6	1.7	−6.1	−21.3	−61.0	−1.8	−6.1

[a] Note: U—nose up, D—nose down, L—nose left, R—nose right, X—horizontal distance from the origin, and Y—vertical distance from the origin.

data and are listed in Table 3. We used the same strain hardening exponent as Warren and Tabbara [15] did for $R_c = 39$ and 37; however, the $R_c = 45$ was found to be less strain rate sensitive, and those parameters were changed. The undeformed density, Young's modulus, and Poisson's ratio of the VAR 4340 $R_c = 45$ steel are taken to be $\rho_p = 8025\,\mathrm{kg/m^3}$ (the actual value is $7830\,\mathrm{kg/m^3}$;

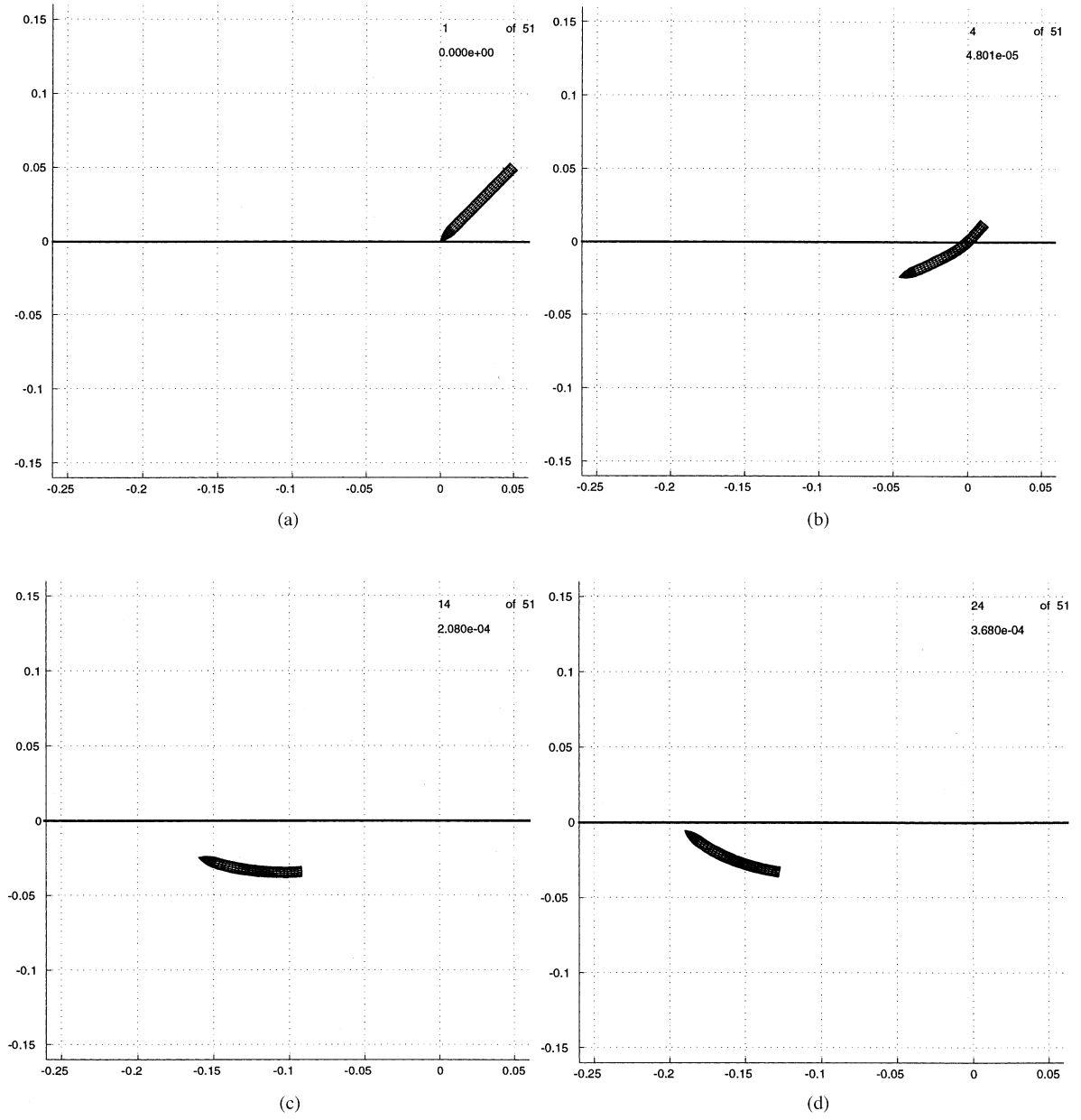

Fig. 10. Simulation with free surface effects for $V_s = 1184\,\mathrm{m/s}$, 45° angle of obliquity, 0.5° pitch up, and 0.75° yaw left: (a) $t = 0\,\mathrm{s}$, (b) $t = 48\,\mu\mathrm{s}$, (c) $t = 208\,\mu\mathrm{s}$, and (d) $t = 368\,\mu\mathrm{s}$.

however, we increased the value slightly to account for mass lost in the discretization process), $E = 206\,\text{GPa}$, and $v = 1/3$, respectively. Fig. 8 compares the stress–strain data obtained by Ravichandran [26] with the results from (20) and show good agreement. Fig. 9 compares the true stress data obtained by Ravichandran [26], and Ramesh [28] at a fixed true strain of 7% with the results from (20) and good agreement is observed over the wide range of strain rates. We also require constants for VAR 4340 $R_c = 44.5$ steel which we obtained by reducing the quasi-static yield strength. This required a change in ε_{p0}; however, all the other parameters remained the same as those obtained for the VAR 4340 $R_c = 45$ steel as shown in Table 3 (it is noted that the quasi-static yield strength in compression is slightly larger than that in tension which is consistent with the results given by Chait [29]).

4. Results and discussion

In this section, we present results from our simulations and compare these with the experimental results. Unless stated otherwise the projectiles for all of the simulations are modeled as VAR 4340 $R_c = 44.5$ steel with 3 CRH ogive-noses that strike 6061-T6511 aluminum targets. Table 4 summarizes the initial conditions obtained from the experiments and final projectile positions in the angle of obliquity plane for both experiment and simulation. Measurements are obtained from the point of impact with the target to the final positions of the nose tip and center of the tail. From the trajectories of the experiments in which the projectile exited the target it was observed that the out of plane displacements (in the yaw direction) were of the order of a few millimeters. This result is consistent with that obtained from the simulations and out of plane displacements will not be considered further.

For all of the simulations we used a Digital Personal Workstation 600 *au*-Series computer with the Digital Unix V4.0D operating system and Digital Fortran compiler. With this system a 300 μs penetration simulation requires approximately 5500 CPU s with the elastic–viscoplastic material

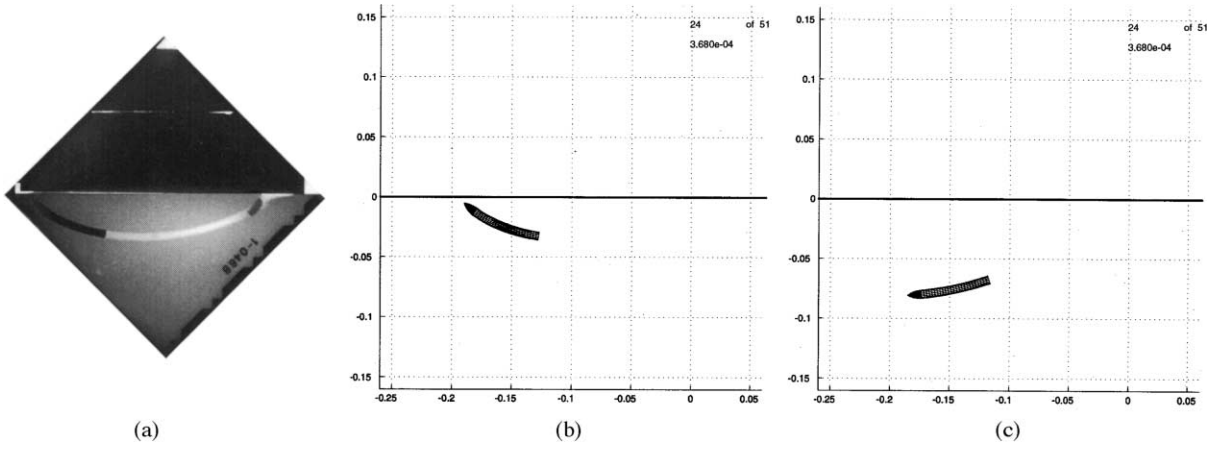

Fig. 11. Final projectile position for $V_s = 1184\,\text{m/s}$, 45° angle of obliquity, 0.5° pitch up, and 0.75° yaw left: (a) post-test radiograph, (b) simulation with free surface effects, and (c) simulation without free surface effects.

model. However, this time came be significantly reduced to approximately 570 CPU s using a simpler elastic-linear hardening material model.

4.1. 45° angle of obliquity

First we consider the case of a projectile striking a target with a striking velocity of 1184 m/s. Images of the simulation that accounts for free surface effects at four specific times are shown in Fig. 10. From these images it is observed that the projectile initially bends and then follows a curved path until it finally comes to rest at approximately 368 μs. In Fig. 11 we compare final projectile configurations obtained from simulations that account for and neglect free surface effects with the post-test radiograph obtained from the corresponding experiment. It is observed that when free surface effects are included the simulation provides a very reasonable prediction of

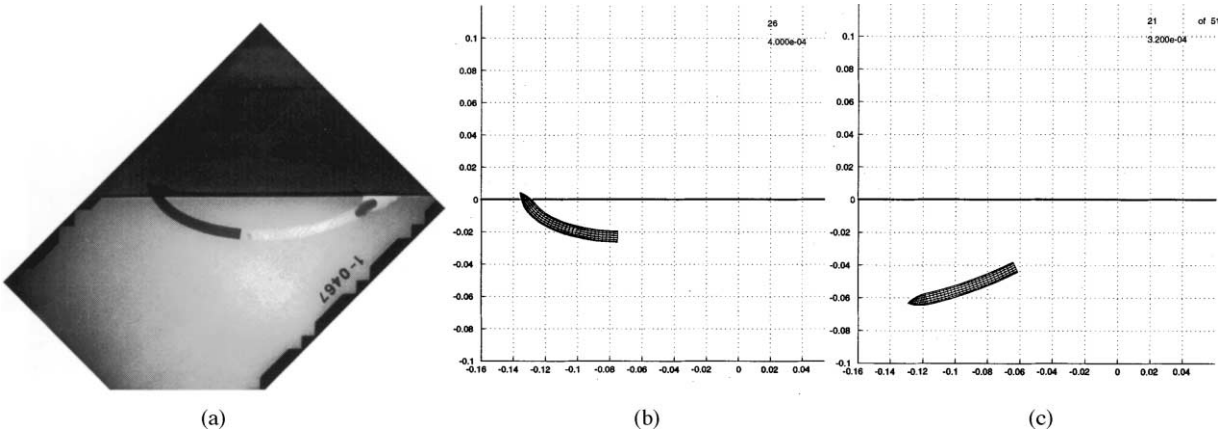

(a) (b) (c)

Fig. 12. Final projectile position for $V_s = 963$ m/s, 45° angle of obliquity, 0.75° pitch up, and 1.0° yaw right: (a) post-test radiograph, (b) simulation with free surface effects, and (c) simulation without free surface effects.

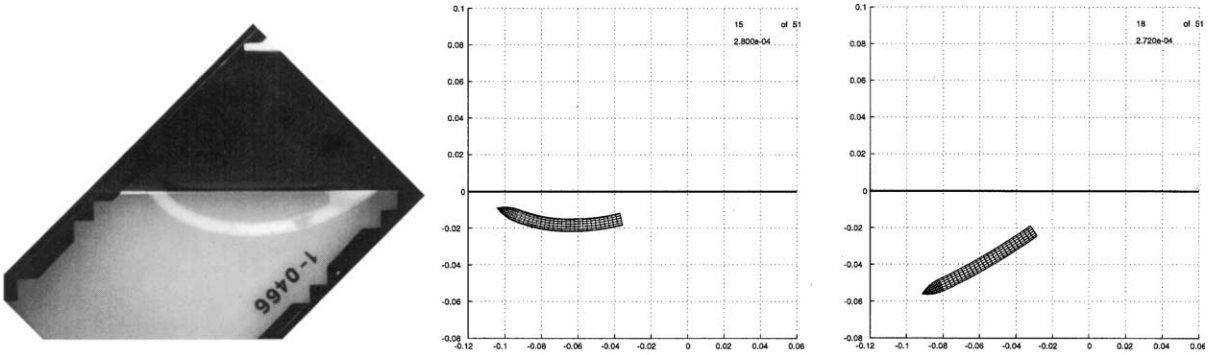

(a) (b) (c)

Fig. 13. Final projectile position for $V_s = 802$ m/s, 45° angle of obliquity, 2.0° pitch up, and 1.5° yaw left: (a) post-test radiograph, (b) simulation with free surface effects, and (c) simulation without free surface effects.

the trajectory and final projectile configuration. However, if the free surface effects are neglected then the projectile will not turn enough because the resistance is greater in the direction of the free surface.

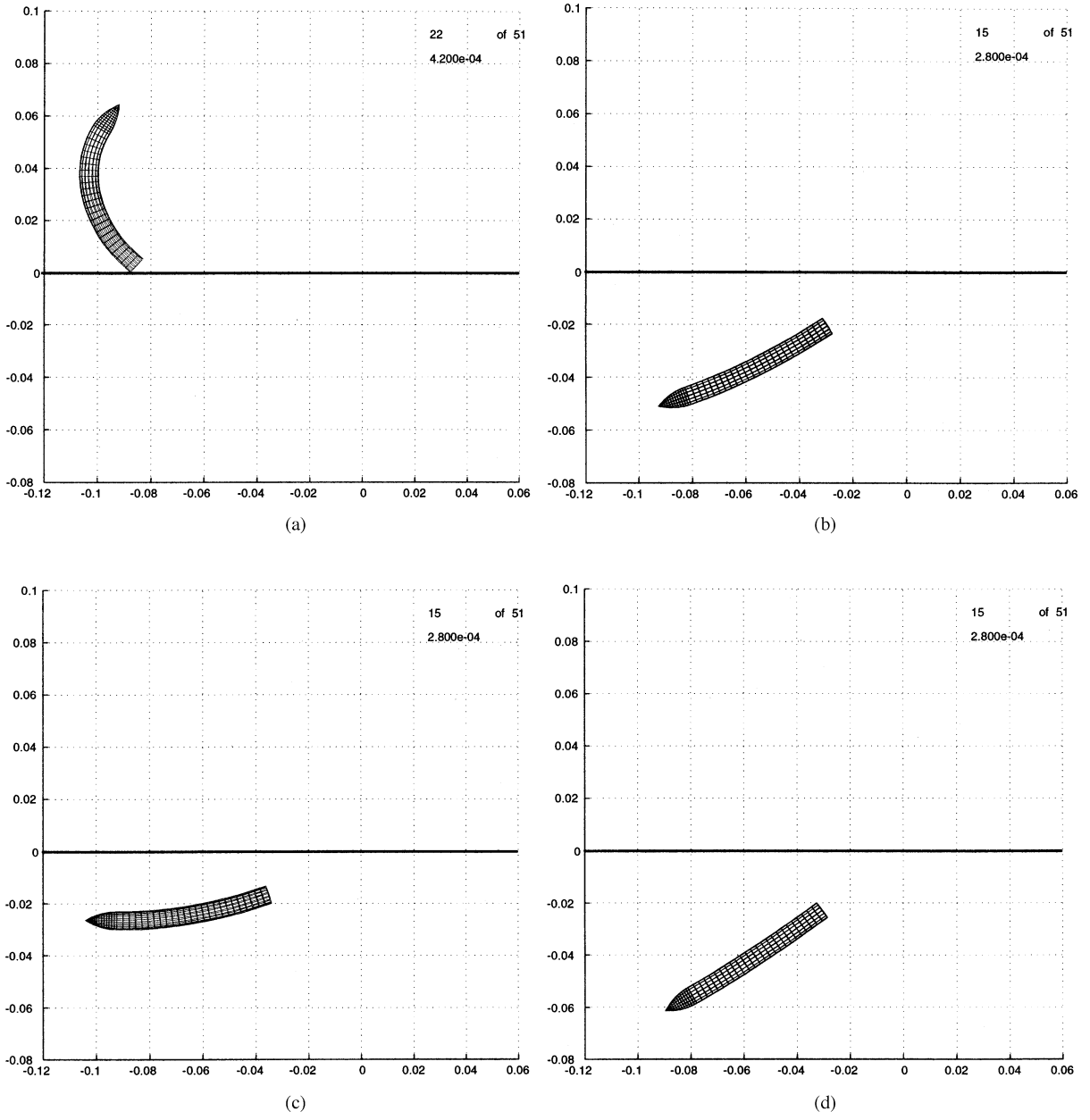

Fig. 14. Simulation of a VAR 4340 ogive-nose projectile penetrating 6061-T6511 aluminum with $V_s = 802\,\mathrm{m/s}$, 45° angle of obliquity, 2.0° pitch up, and 1.5° yaw left: (a) $R_c = 42$ with free surface effects (b) $R_c = 42$ without free surface effects (c) $R_c = 47$ with free surface effects (d) $R_c = 47$ without free surface effects.

Next, we consider the case of a projectile striking a target with a velocity of 963 m/s. In Fig. 12 we compare final projectile configurations obtained from simulations with and without free surface effects to the corresponding experimental results. In this case the projectile just barely breaks through the surface of the target at the end of its trajectory. Again, the simulation that

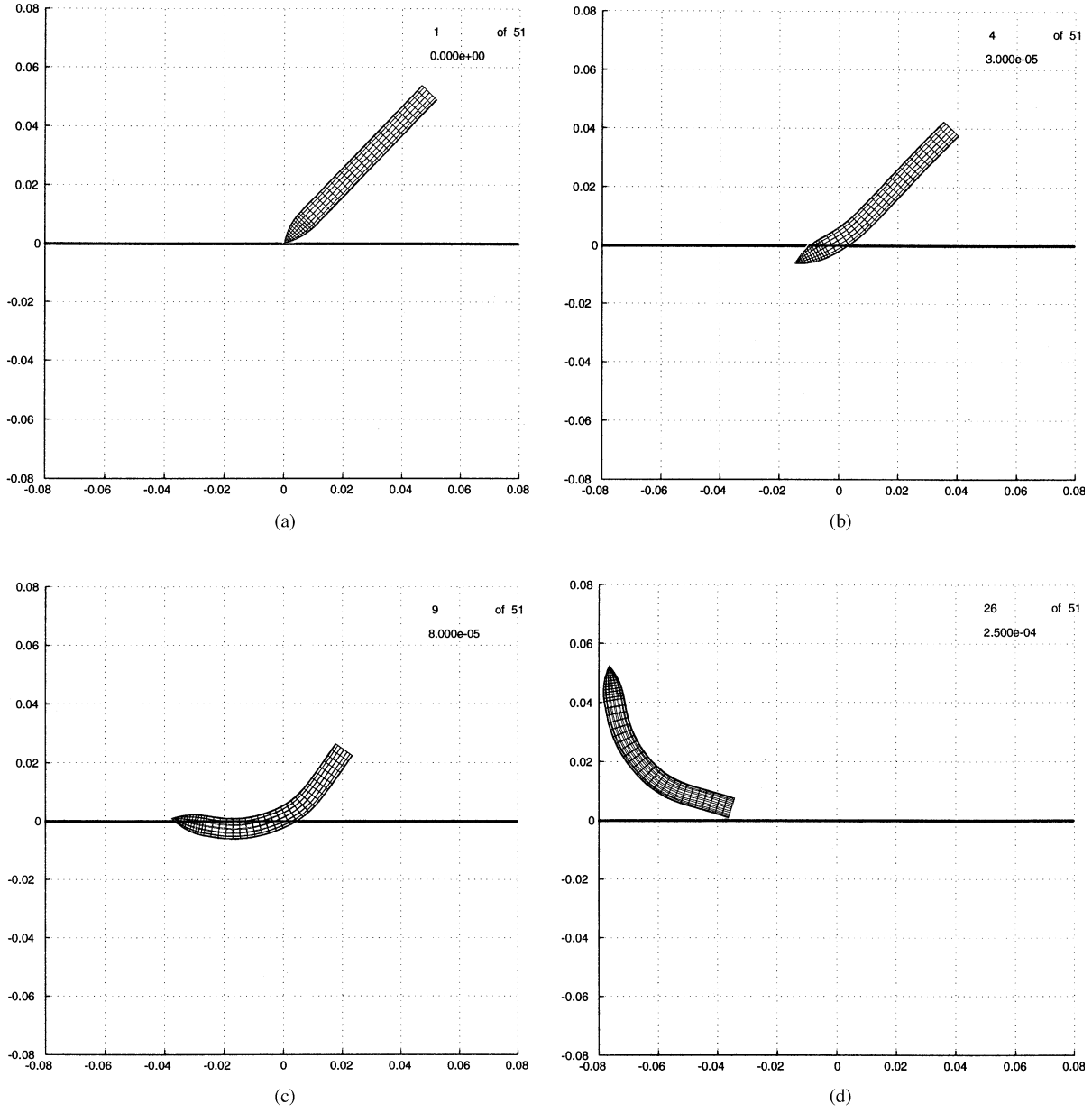

Fig. 15. Simulation with free surface effects for $V_s = 553$ m/s, 45° angle of obliquity, 1.25° pitch up, and 0.75° yaw right: (a) $t = 0$ s, (b) $t = 30\,\mu$s, (c) $t = 80\,\mu$s, and (d) $t = 250\,\mu$s.

accounts for free surface effects does a very good job of predicting both the trajectory and final projectile configuration.

In Fig. 13 we compare our simulations with the experimental results for a projectile striking a target with a velocity of 802 m/s. For this case the projectile exited the face of the target approximately 100 mm from the point of impact. A post-test examination of the projectile revealed a thin covering of aluminum deposited over the steel surface. This thin layer increased the pre-test mass of the projectile by 1.5 mg. The simulation which includes free surface effects predicts the projectile will come to rest just below the face of the target which is a little short of what actually occurred but still much closer than the simulation that neglects free surface effects. For this particular case we illustrate the effect of projectile strength on trajectory by decreasing and increasing the quasi-static yield strength of the projectile by 100 MPa. This is equivalent to Rockwell hardnesses of $R_c = 42$ and 47, respectively. Final projectile configurations obtained from simulations with and without free surface effects for $R_c = 42$ and 47 projectiles are shown in Fig. 14. It is observed in Fig. 14a that the projectile exits the face of the target at approximately 90 mm from the point of impact, which is consistent with the experiment. The results in Fig. 14 indicate that decreasing the projectile yield strength by approximately 7% has a dramatic effect on the trajectory when the projectile is near the free surface. This is due to the fact that the projectile exhibits less resistance to bending when the strength is decreased and when coupled with the free surface effect causes it to rotate more and exit the target. Similar results are also observed if the target strength is increased, in which case the projectile will bend more and exit the target face.

Images at four specific times are shown in Fig. 15 of the simulation which accounts for free surface effects for a projectile striking a target with a velocity of 553 m/s. For this case the projectile initially bends significantly and essentially ricochets from the face of the target approximately 38 mm from the point of impact. In Fig. 16 we compare final projectile configurations obtained from simulations that account for and neglect free surface effects with the post-test radiograph obtained from the corresponding experiment. As with the previous case, a thin layer of aluminum was deposited over surface of the projectile in the experiment and

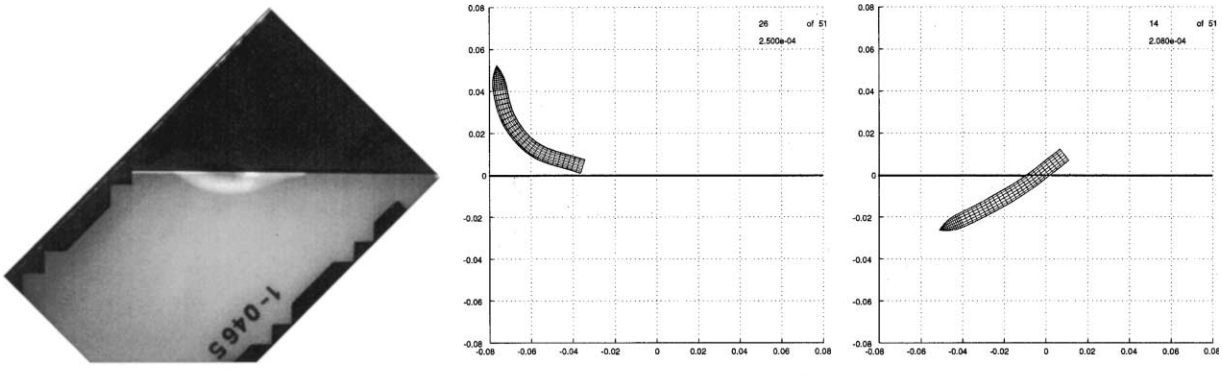

Fig. 16. Final projectile position for $V_s = 553$ m/s, 45° angle of obliquity, 1.25° pitch up, and 0.75° yaw right: (a) post-test radiograph, (b) simulation with free surface effects, and (c) simulation without free surface effects.

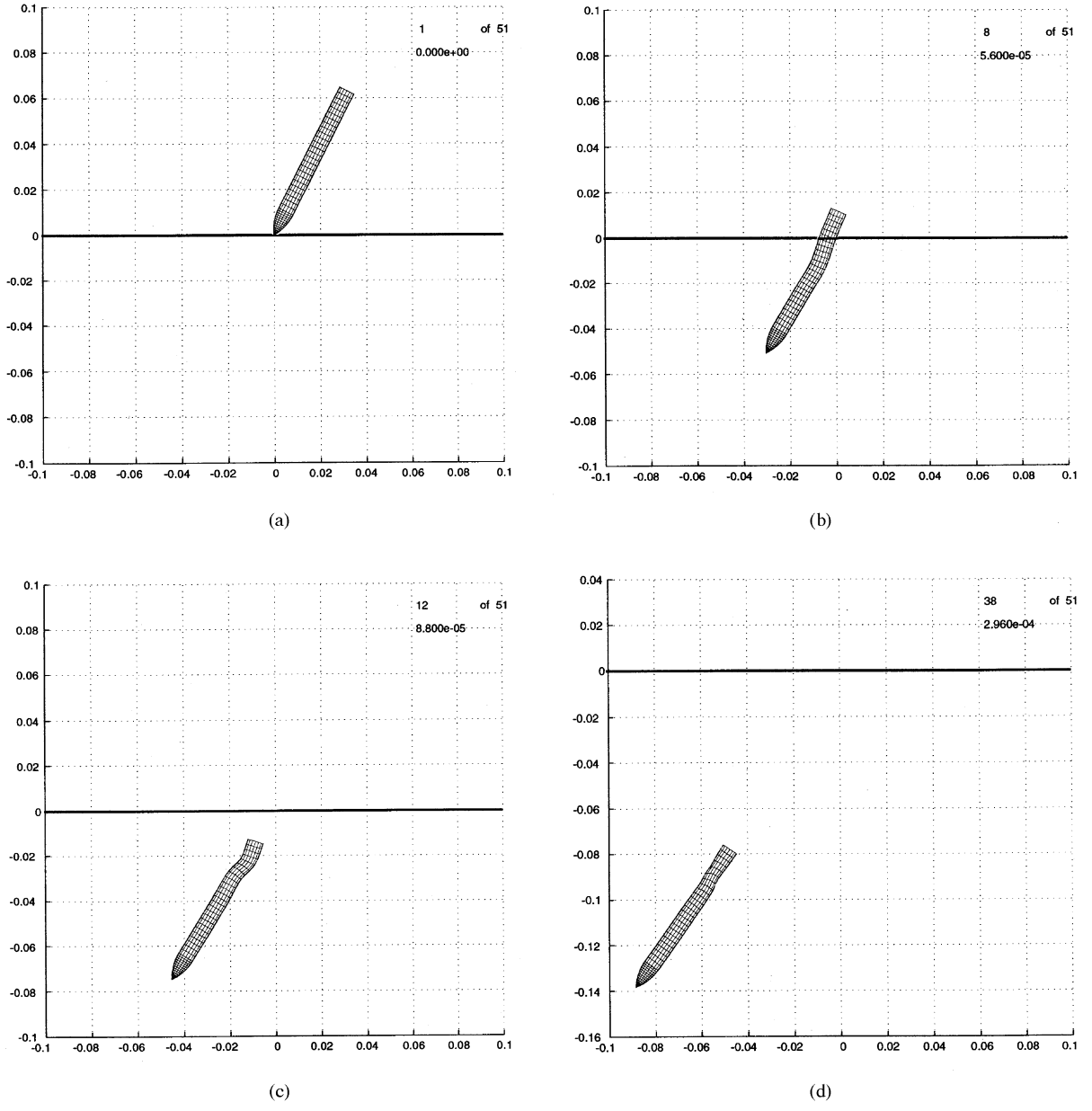

Fig. 17. Simulation with free surface effects for $V_s = 1156\,\text{m/s}$, 30° angle of obliquity, 3.25° pitch up, and 0° yaw: (a) $t = 0\,\text{s}$, (b) $t = 50\,\mu\text{s}$, (c) $t = 88\,\mu\text{s}$, and (d) $t = 296\,\mu\text{s}$.

increased its pre-test mass by 5.7 mg. When free surface effects are neglected, the simulation does not predict the ricochet effect that is observed experimentally and with the simulation in Fig. 15.

These results illustrate that the free surface has a significant effect on the trajectory of steel projectiles striking aluminum targets with a 45° angle of obliquity over a wide range of striking

velocities. It is also observed that as striking velocity is increased the projectile enters the target quicker, which reduces the amount of initial bending that it undergoes. This causes the projectile to stay in the target longer and at the higher velocities the projectile will not exit the face of the target.

4.2. 30° angle of obliquity

Images at four specific times are shown in Fig. 17 of the simulation which accounts for free surface effects for a projectile striking a target with a velocity of 1156 m/s. This particular case had the largest measured pitch and it is observed in the simulation that the tail of the projectile

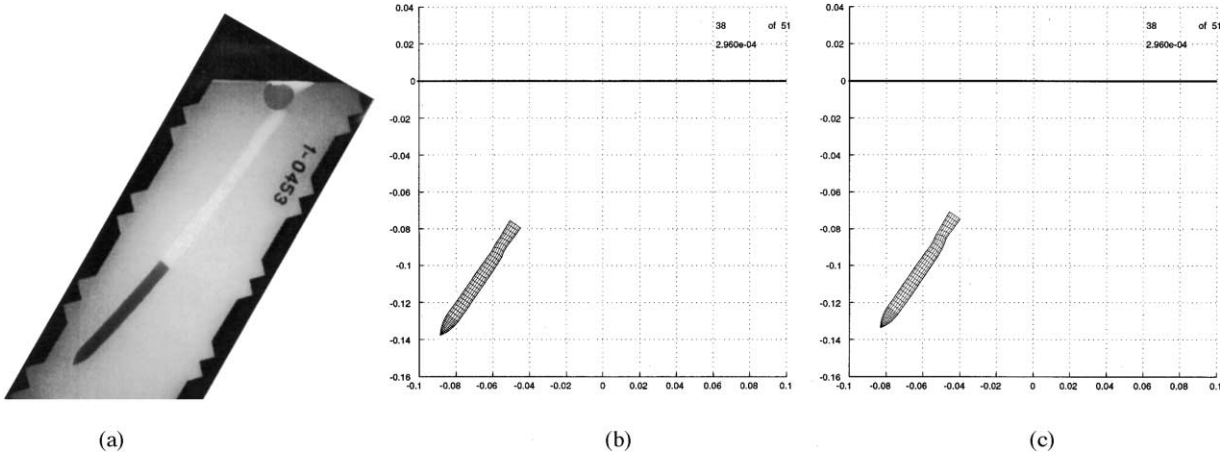

Fig. 18. Final projectile position for $V_s = 1156$ m/s, 30° angle of obliquity, 3.25° pitch up, and 0° yaw: (a) post-test radiograph (b) simulation with free surface effects, and (c) simulation without free surface effects.

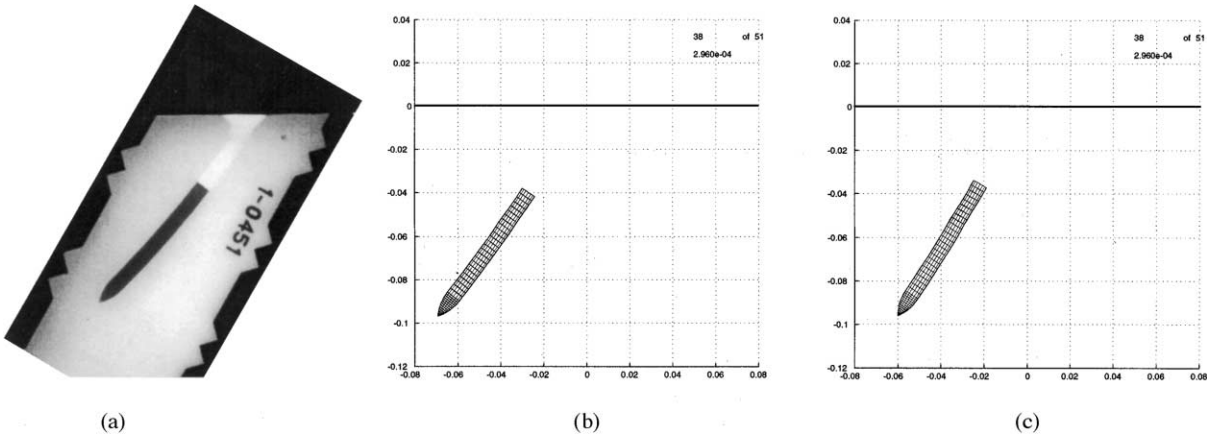

Fig. 19. Final projectile position for $V_s = 853$ m/s, 30° angle of obliquity, 2.75° pitch up, and 0.75° yaw left: (a) post-test radiograph, (b) simulation with free surface effects, and (c) simulation without free surface effects.

violently whips back and forth as it proceeds through the target and sustains significant plastic deformation. In Fig. 18 we compare final projectile configurations obtained from simulations that account for and neglect free surface effects with the post-test radiograph obtained from the corresponding experiment. Both of the simulations exhibit the notable tail motion with plastic deformation. Effects of tail bending are also observed in the channel of the post-test radiograph. With this high velocity and large angle of inclination the tail whips back and forth well into the tunneling region. For this situation the simulation method loses accuracy and under predicts the final depth of penetration. As discussed earlier, the reason for this is due to the fact the current cavity expansion algorithm applies a load on the shank whenever there is a component of velocity

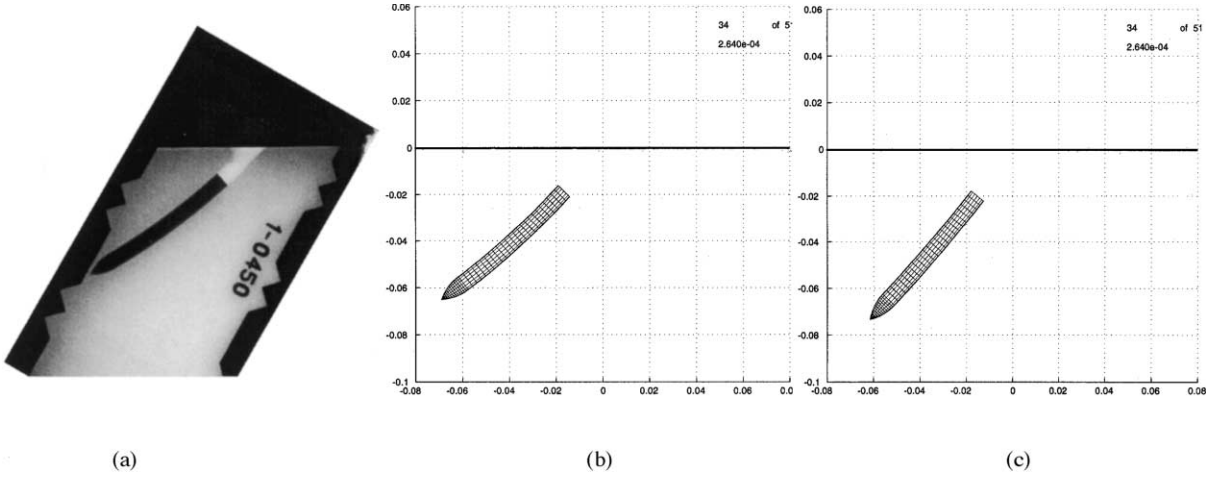

(a) (b) (c)

Fig. 20. Final projectile position for $V_s = 753\,\text{m/s}$, 30° angle of obliquity, 0.75° pitch down, and 0.25° yaw left: (a) post-test radiograph, (b) simulation with free surface effects, and (c) simulation without free surface effects.

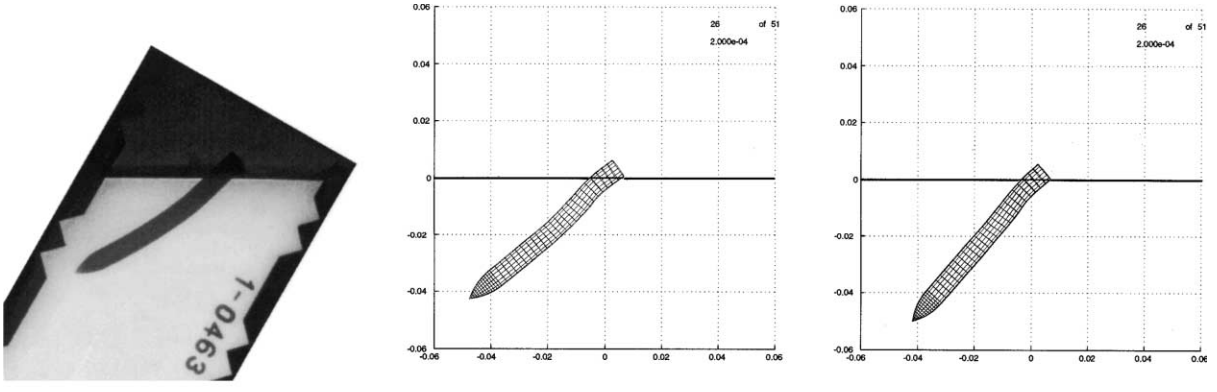

(a) (b) (c)

Fig. 21. Final projectile position for $V_s = 577\,\text{m/s}$, 30° angle of obliquity, 0.5° pitch down, and 0.75° yaw left: (a) post-test radiograph, (b) simulation with free surface effects, and (c) simulation without free surface effects.

in the outward normal direction and does not account for material that has been moved out of the way in the tunneling region. It is also noticed in both simulations that the final projectile positions are very close with the case with free surface effects only going slightly further in both the vertical and horizontal directions.

In Figs. 19–21 we compare our simulations with the experimental results for projectiles striking targets with velocities of 853, 753, and 577 m/s, respectively. For these three cases the simulations that include free surface effects cause the projectile to travel further in the horizontal direction and less in the vertical direction than when free surface effects are neglected. The final projectile positions with free surface effects are in good agreement with the experimental results in the horizontal direction; however, they slightly over predict the depth in the vertical direction, which indicates that the projectile in the simulation is not rotating quite enough. This can possibly be attributed to the fact that we are neglecting thermal effects from both heat transferring into the projectile from the target along with adiabatic heating of the projectile from its own plastic deformation. Both of these thermal mechanisms will cause the projectile to soften and bend more causing greater rotation. From these results it is observed that free surface effects are important for predicting the trajectory; however, the effect is not as significant as at 45°.

4.3. 15° angle of obliquity

In Figs. 22–25 we compare our simulations with the experimental results for projectiles striking targets with velocities of 1209, 985, 759, and 590 m/s, respectively. For these four cases it is observed that the free surface effect has less of an influence on the trajectory than the cases with 30° and 45° angles of obliquity. In fact, for striking velocities of 1209 and 985 m/s the simulations that neglect free surface effects attain slightly larger distances in the horizontal direction than the

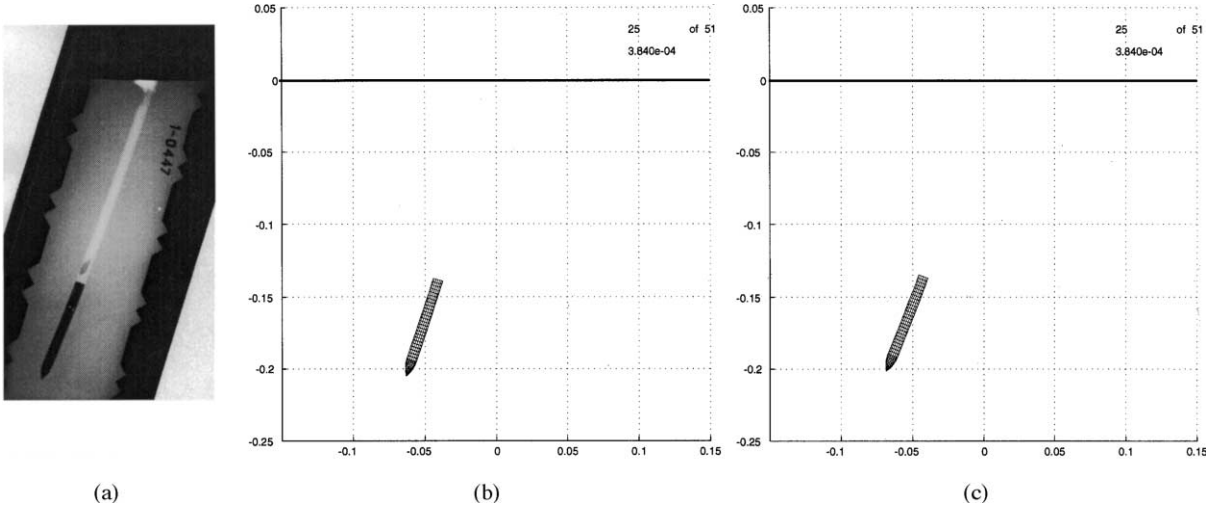

Fig. 22. Final projectile position for $V_s = 1209$ m/s, 15° angle of obliquity, 0.75° pitch up, and 0.5° yaw left: (a) post-test radiograph, (b) simulation with free surface effects, and (c) simulation without free surface effects.

simulations that include free surface effects giving a result that is a slightly closer to that obtained experimentally.

5. Summary

In this paper we have presented the results from a series of depth-of-penetration experiments in which VAR 4340 $R_c = 44.5$ steel ogive-nosed projectiles were launched into 6061-T6511 aluminum

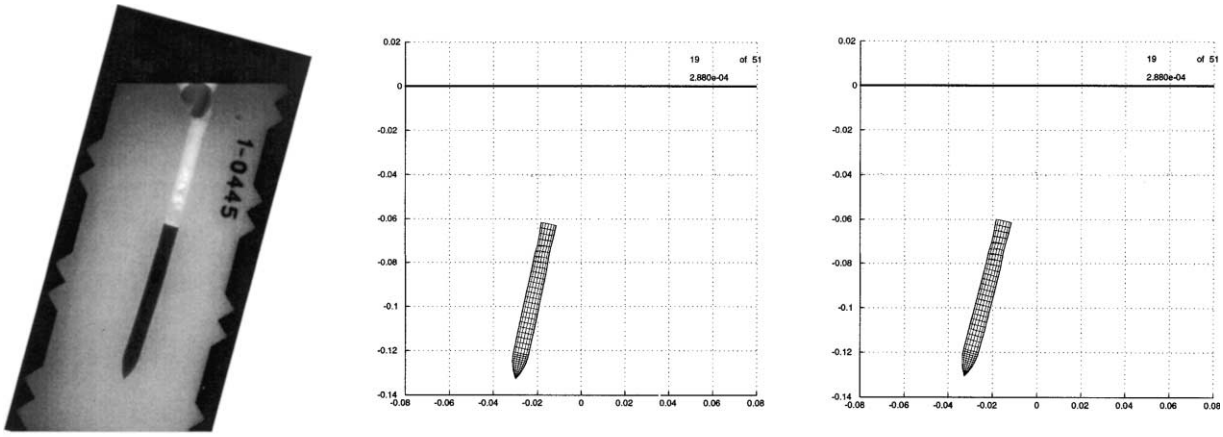

(a) (b) (c)

Fig. 23. Final projectile position for $V_s = 985$ m/s, 15° angle of obliquity, 2.5° pitch up, and 0.75° yaw left: (a) post-test radiograph, (b) simulation with free surface effects, and (c) simulation without free surface effects.

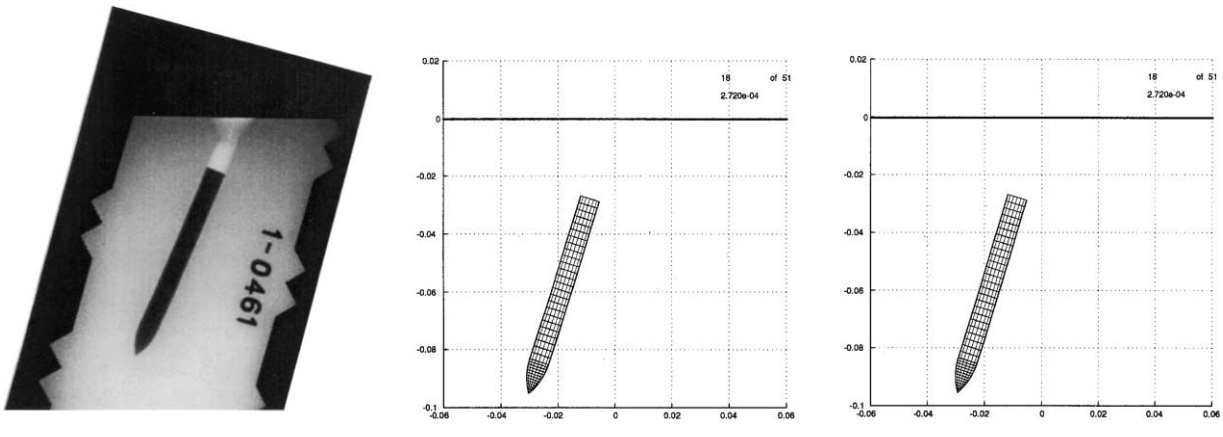

(a) (b) (c)

Fig. 24. Final projectile position for $V_s = 759$ m/s, 15° angle of obliquity, 0.5° pitch up, and 0.75° yaw left: (a) post-test radiograph, (b) simulation with free surface effects, and (c) simulation without free surface effects.

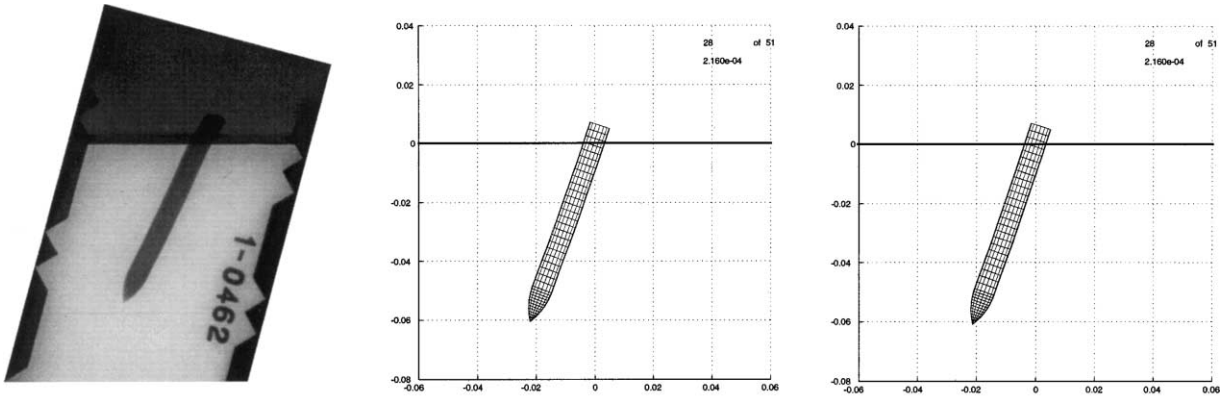

Fig. 25. Final projectile position for $V_s = 590\,\mathrm{m/s}$, 15° angle of obliquity, 0.5° pitch down, and 0.5° yaw right: (a) post-test radiograph, (b) simulation with free surface effects, and (c) simulation without free surface effects.

targets at oblique angles. Next, we conducted simulations of the penetration experiments in order to validate the use of experimentally verified analytical functions to represent the target resistance in ballistic events. Comparison with experimental results indicates that over a wide range of striking velocities this method allows for the accurate prediction of the trajectory and permanent projectile deformation provided the projectile does not deform excessively and free surface effects are accounted for with increasing angle of obliquity. Thus, for the class of problems within the realm of assumptions considered here, this technique is efficient and robust and can be included in a broader software tool which can be utilized for design purposes. Furthermore, it has been recently shown by Danielson and Adley [30] that this method exhibits excellent scalability in a parallel computing architecture.

Acknowledgements

This work was supported by the United States Department of Energy and the Joint DoD/DOE Munitions Technology Development Program. Sandia is a multiprogram laboratory operated by Sandia Corporation, a Lockheed Martin Company, for the United States Department of Energy under Contract DE-AC04-94AL85000. The authors also gratefully acknowledge numerous discussions with M.D. Adley, T.A. Duffy, M.J. Forrestal, D.B. Loncope, R.W. Macek, A.J. Piekutowski, K.T. Ramesh, G. Ravichandran, and M.R. Tabbara.

References

[1] Goldsmith W. Non-ideal projectile impact on targets. Int J Impact Eng 1999;22:95–395.
[2] Bishop RF, Hill R, Mott NF. The theory of indentation and hardness. Proc Roy Soc 1945;57(3):147–59.

[3] Goodier JN. On the mechanics of indentation and cratering in the solid targets of strain-hardening metal by impact of hard and soft spheres. Proceedings of the Seventh Symposium on Hypervelocity Impact III. New York: AIAA, 1965. p. 215–59.
[4] Hill R. A theory of earth movement near a deep underground explosion. Memo No. 21–48, Armament Research Establishment, Fort Halstead, Kent, UK, 1948.
[5] Hill R. The mathematical theory of plasticity. London: Oxford University Press, 1950.
[6] Hopkins HG. Dynamic expansion of spherical cavities in metals. In: Sneddon I, Hill R, editors. Progress in solid mechanics, vol. 1. New York: North Holland, 1960. p. 5–164.
[7] Forrestal MJ, Okajima K, Luk VK. Penetration of 6061-T651 aluminum targets with rigid long rods. ASME J Appl Mech 1988;55:755–60.
[8] Forrestal MJ, Brar NS, Luk VK. Penetration of strain-hardening targets with rigid spherical-nose rods. ASME J Appl Mech 1991;58:7–10.
[9] Forrestal MJ, Tzou DY, Askari E, Longcope DB. Penetration into ductile metal targets with rigid spherical-nose rods. Int J Impact Eng 1995;16:699–710.
[10] Warren TL, Forrestal MJ. Effects of strain hardening and strain-rate sensitivity on the penetration of aluminum targets with spherical-nosed rods. Int J Solids Struct 1998;35:3737–53.
[11] Piekutowski AJ, Forrestal MJ, Poormon KL, Warren TL. Penetration of 6061-T6511 aluminum targets by ogive-nose steel projectiles with striking velocities between 0.5 and 3.0 km/s. Int J Impact Eng 1999;23: 723–34.
[12] Roisman IV, Weber K, Yarin AL, Hohler V, Rubin MB. Oblique penetration of a rigid projectile into a thick elastic–plastic target: theory and experiment. Int J Impact Eng 1999;22:707–26.
[13] Roisman IV, Yarin AL, Rubin MB. Oblique penetration of a rigid projectile into an elastic–plastic target. Int J Impact Eng 1997;19:769–95.
[14] Zukas JA. High velocity impact dynamics. New York: Wiley, 1990.
[15] Warren TL, Tabbara MR. Simulations of the penetration of 6061-T6511 aluminum targets by spherical-nosed VAR 4340 steel projectiles. Int J Solids Struct 2000;37:4419–35.
[16] Forrestal MJ, Piekutowski AJ. Penetration experiments with 6061-T6511 aluminum targets and spherical-nose steel projectiles at striking velocities between 0.5 and 3.0 km/s. Int J Impact Eng 2000;24:57–67.
[17] Warren TL, Tabbara MR. Spherical cavity-expansion forcing function in PRONTO 3D for application to penetration problems. SAND97-1174, Sandia National Laboratories, Albuquerque, NM, 1997.
[18] Camacho GT, Ortiz M. Adaptive Lagrangian modeling of ballistic penetration of metallic targets. Comput Meth Appl Mech Eng 1997;142:269–301.
[19] Macek RW, Duffey TA. Finite cavity expansion method for near-surface effects and layering during earth penetration. Int J Impact Eng 2000;24:239–58.
[20] Longcope DB, Tabbara MR, Jung J. Modeling of oblique penetration into geologic targets using cavity expansion penetrator loading with target free-surface effects. SAND99-1104, Sandia National Laboratories, Albuquerque, NM, 1999.
[21] Brown WF, Mindlin H, Ho CY. Aerospace structural metals handbook, vol. 1. Code 1206, CINDAS/USAF CRDA Handbooks Operation, Purdue University, West Lafayette, IN, 1996.
[22] Forrestal MJ, Luk VK, Brar NS. Penetration of aluminum armor plates with conical-nose projectiles. Mech Mater 1990;10:97–105.
[23] Forrestal MJ, Luk VK. Dynamic spherical cavity-expansion in a compressible elastic–plastic solid. ASME J Appl Mech 1988;55:275–9.
[24] Taylor LM, Flanagan DP. PRONTO 3D a three-dimensional transient solid Dynamics Program. SAND87-1912, Sandia National Laboratories, Albuquerque, NM, 1989.
[25] Peirce D, Shih CF, Needleman A. A tangent modulus method for rate dependent solids. Comp Struct 1984;18: 875–87.
[26] Ravichandran G. Mechanical testing of 6061-T651 aluminum alloy and 4340 steel. Private communication, California Institute of Technology, Pasadena, CA, 1997.
[27] Ramesh KT, Narasimhan S. Finite deformations and the dynamic measurement of radial strains in compression Kolsky bar experiments. Int J Solids Struct 1996;33:3723–38.

[28] Ramesh KT. High strain rate behavior in 4340 steel. Private communication, The Johns Hopkins University, Baltimore, MD, 1997.
[29] Chait R. Factors influencing the strength differential of high strength steels. Met Trans A 1972;3:365–71.
[30] Danielson KT, Adley MD. A meshless treatment of three-dimensional penetrator targets for parallel computation. Comput Mech 2000;25:267–73.